# Including antenna mispointing in a semi-analytical model for delay/Doppler altimetry

Abderrahim Halimi, Corinne Mailhes, Jean-Yves Tourneret, François Boy, Thomas Moreau

# Including Antenna Mispointing in a Semi-Analytical Model for Delay/Doppler Altimetry

Abderrahim Halimi, *Member, IEEE*, Corinne Mailhes, *Member, IEEE*,
Jean-Yves Tourneret, *Senior Member, IEEE*, Francois Boy, and Thomas Moreau

*Abstract*—Delay/Doppler altimetry (DDA) aims at reducing the measurement noise and increasing the along-track resolution in comparison with conventional pulse-limited altimetry. In a previous paper, we have proposed a semi-analytical model for DDA, which considers some simplifications as the absence of mispointing antenna. This paper first proposes a new analytical expression for the flat surface impulse response (FSIR), considering antenna mispointing angles, a circular antenna pattern, no vertical speed effect, and uniform scattering. The 2-D delay/Doppler map is then obtained by a numerical computation of the convolution between the proposed analytical function, the probability density function of the heights of the specular scatterers, and the time/frequency point target response of the radar. The approximations used to obtain the semi-analytical model are analyzed, and the associated errors are quantified by analytical bounds for these errors. The second contribution of this paper concerns the estimation of the parameters associated with the multilook semi-analytical model. Two estimation strategies based on the least squares procedure are proposed. The proposed model and algorithms are validated on both synthetic and real waveforms. The obtained results are very promising and show the accuracy of this generalized model with respect to the previous model assuming zero antenna mispointing.

*Index Terms*—Altimetry, antenna mispointing, Cryosat-2, delay/Doppler map (DDM), least squares (LS) estimation, SAR altimetry.

## I. INTRODUCTION

**D**ELAY/Doppler altimetry (DDA) has been receiving an increasing interest in the literature [1]–[5]. Following [6]–[9], a modification of a TOPEX-type altimeter with onboard processing was studied in [1] leading to DDA which is pulse-limited across-track and beam-limited along-track. This new technology aims at reducing the measurement noise (speckle noise) and increasing the along-track resolution (i.e., reducing the size of the along-track cell after Doppler processing) in comparison with conventional pulse-limited altimetry. Speckle reduction is obtained by increasing the number of observations, which allows providing better precision and estimation of the

A. Halimi, C. Mailhes, and J.-Y. Tourneret are with the IRIT/INP-ENSEEIHT/TéSA, University of Toulouse, 31071 Toulouse Cedex 7, France (e-mail: Abderrahim.Halimi@enseeiht.fr; Corinne.Mailhes@enseeiht.fr; Jean-Yves.Tourneret@enseeiht.fr).

F. Boy is with the Centre National d'Études Spatiales, 31401 Toulouse Cedex 9, France (e-mail: Francois.Boy@cnes.fr).

T. Moreau is with Collecte Localisation Satellite, 31520 Ramonville Saint-Agne, France (e-mail: tmoreau@cls.fr).

physical parameters of interest. Enhancing the parameter quality is an important issue that has been receiving considerable attention in the altimetry community. Many studies related to conventional altimetry (CA) have been devoted to improve the well-known Brown model [10] in terms of quality of estimation [11]–[13]. On the other hand, the increase of resolution in DDA is achieved by using the information contained in the Doppler frequency (related to the satellite velocity). This resolution improvement can be advantageously exploited to process altimetric measurements closer to the coast (note that the processing of coastal waveforms has received some recent attention in the literature [14]–[17]). Indeed, one can expect to extract useful information from oceanic cells located up to 300 m from the coast, whereas the minimum accepted distance is about 10 km for CA.

As in CA, the mean power of a delay/Doppler echo is expressed by a convolution of three terms that are the probability density function (PDF) of the heights of the specular scatterers, the time/frequency point target response (PTR) of the radar, and the flat surface impulse response (FSIR) [18], [19]. The first term, i.e., $PDF(t)$, is considered as a zero-mean Gaussian function whose standard deviation is related to the significant wave height (SWH) parameter [10], [13]. The second term, i.e., PTR, can be measured as explained in [20] and is well approximated by a product of two sine cardinal terms as in [18], [21], and [22]. The third term, i.e., FSIR, includes the shape information about the resulting altimetric echo. This term has been numerically approximated in [4] and [23], whereas an analytical model was proposed in [22]. However, the model in [22] was developed with simplifying assumptions and did not consider any antenna mispointing, which may lead to reduced estimation performance in practical applications. Note also that the previous terms could be jointly evaluated as presented in [3], which provided an integral expression including the FSIR and the effect of the azimutal processing while considering a Gaussian approximation for the Doppler PTR. However, the assumption of a Gaussian PTR might reduce the estimation performance as already observed in CA [24], [25].

The first contribution of this paper is the derivation of a generalized analytical model for the FSIR that accounts for antenna mispointing. The proposed analytical expression for the FSIR also considers Earth curvature, a circular antenna pattern and a Gaussian approximation for the antenna gain as in [10], [22]. This analytical expression is established using two approximations that are analyzed and justified by deriving an upper bound for the error between the exact FSIR and its approximation. The 2-D delay/Doppler map (DDM) is then obtained by a numerical

convolution between the proposed analytical FSIR expression, the PDF of the sea wave heights, and the time/frequency PTR. The resulting DDM depends on five altimetric parameters: epoch $\tau$, SWH, amplitude $P_u$, along-track mispointing angle $\xi_{\mathrm{al}}$, and across-track mispointing angle $\xi_{\mathrm{ac}}$. Appropriate processing, including range migration and multilooking, is applied to the resulting DDM, yielding the multilook echo. The behavior of this echo is analyzed as a function of the direction of antenna mispointing. Since the mispointing has a different behavior on beam-limited and pulse-limited altimetry [26], [27], the study separates along- and across-track mispointing angles.

The second contribution of this work is the derivation of estimators for the parameters associated with the previously derived multilook echo. This paper considers a least squares (LS) technique as in [18], [21], [22], [28], and [29] based on a Levenberg–Marquardt algorithm for parameter estimation. Since the antenna mispointing results in high correlation between the along-track mispointing and the echo's amplitude, a four-parameter estimation strategy is proposed to reduce the number of parameters to estimate (initially equal to five). To evaluate the different LS strategies, we compare their estimation performance to the model in [22] (involving three parameters only). The proposed model and algorithms are validated with simulated and real Cryosat-2 data. The obtained results are very promising and confirm the accuracy of the proposed model.

This paper is organized as follows. Section II presents the proposed generalized semi-analytical model for DDA and analyzes its behavior as a function of antenna mispointing. The LS estimation algorithm and the criteria used for its validation are introduced in Section III. Section IV justifies the approximations used to obtain the analytical FSIR. The proposed model and estimation algorithms are also validated using simulated and real Cryosat-2 data. Conclusions and future work are finally reported in Section V.

## II. SEMI-ANALYTICAL MODEL FOR DDA

This section introduces the proposed semi-analytical model for delay/Doppler waveforms. The interest of this model compared with the previously published model [22] is that it includes parameters related to antenna mispointing.

### A. Delay/Doppler Convolution Model

The mean power of a delay/Doppler echo can be expressed as the convolution of three terms: the time/frequency FSIR, the PDF of the heights of the specular scatterers, and the time/frequency PTR of the radar as follows [18], [19]:

$$P(t, f) = \mathrm{FSIR}(t, f) * \mathrm{PDF}(t) * \mathrm{PTR}(t, f) \qquad (1)$$

with

$$\mathrm{PDF}(t) = \frac{1}{\sqrt{2\pi}\sigma_s} \exp\left(-\frac{t^2}{2\sigma_s^2}\right) \qquad (2\mathrm{a})$$

$$\mathrm{PTR}(t, f) = \mathrm{PTR}_T(t)\mathrm{PTR}_F(f) \qquad (2\mathrm{b})$$

$$\mathrm{PTR}_T(t) = \left|\frac{\sin\left(\pi\frac{t}{T}\right)}{\pi\frac{t}{T}}\right|^2, \quad \mathrm{PTR}_F(f) = \left|\frac{\sin\left(\pi\frac{f}{F}\right)}{\pi\frac{f}{F}}\right|^2 \qquad (2\mathrm{c})$$
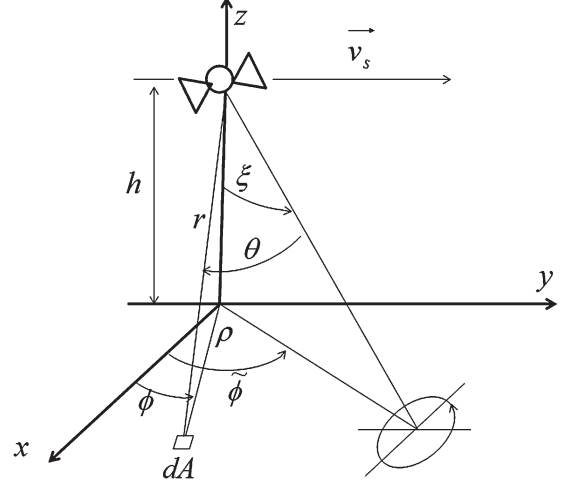


Fig. 1.   Geometry for the FSIR.

where $t$ is the two-way incremental ranging times expressed as $t = t' - (2h/c)$, with $t'$ the travel time of the echo from the instant of transmission, $h$ is the altitude of the satellite, $c$ is the speed of light, $T$ is the sampling period, $F$ is the frequency resolution, and $\sigma_s$ is linked to the SWH by $\sigma_s = \mathrm{SWH}/2c$ (an extended glossary of notations is available in [30]). Note that the PDF can be generalized to account for wave asymmetry [11] and that a measured PTR can be used. The proposed analytical expression for the first term (FSIR) is described in the following section.

### B. Proposed Analytical Model for FSIR

In CA, the FSIR depends only on time and is obtained by integrating the power of the backscattered altimetric echo over the illuminated area of the surface as follows [10]:

$$\mathrm{FSIR}(t') = \frac{\lambda^2}{(4\pi)^3 L_p} \int_{\mathbb{R}^+ \times [0, 2\pi[} \frac{\delta\left(t' - \frac{2r}{c}\right) G^2(\rho, \phi)\sigma^0}{r^4} \rho d\rho d\phi \qquad (3)$$

where $\rho$ are $\phi$ are the radius and the angle representing the polar coordinates, $r = \sqrt{\rho^2 + h^2}$ is the range between the satellite and the observed surface as shown in Fig. 1, $\delta(t)$ is the Dirac delta function, $G$ is the power gain of the radar antenna, $\sigma_0$ is the backscatter coefficient of the surface,[1] $\lambda$ is the wavelength, and $L_p$ is the two-way propagation loss.

The DDA was proposed to increase the along-track resolution by considering the Doppler effect resulting from the satellite velocity. The corresponding FSIR is then obtained by integrating over each Doppler beam. The $n$th Doppler beam at time instant $t$ depicted in Fig. 2 is characterized by an angle $\phi$ varying in the interval $D_{t,n} = [\phi_{t,n}, \phi_{t,n+1}] \cup [\phi'_{t,n}, \phi'_{t,n+1}]$, leading to

$$\mathrm{FSIR}(t', n) = \frac{\lambda^2}{(4\pi)^3 L_p} \int_{\mathbb{R}^+ \times D_{t,n}} \frac{\delta\left(t' - \frac{2r}{c}\right) G^2(\rho, \phi)\sigma^0}{r^4} \rho d\rho d\phi. \qquad (4)$$

---

[1]This coefficient may change in the observed scene [31] even if it is considered as a constant in this paper for simplicity.
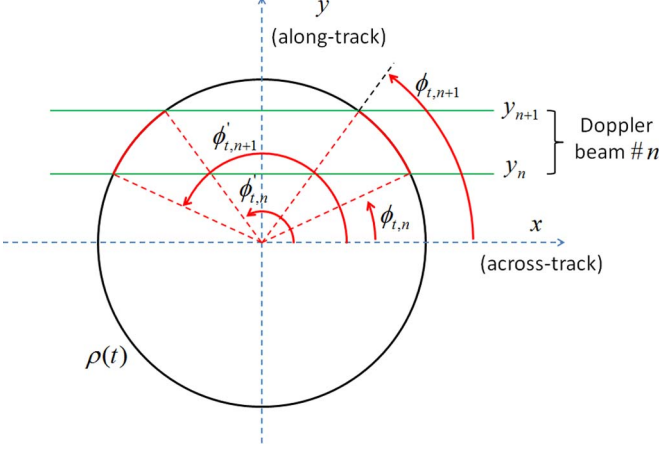
Fig. 2. Integrating angles for specific circle of propagation and Doppler beam.

The integral with respect to $\rho$ in (4) can be analytically computed by considering $(ct/h) \ll 1$ and a Gaussian approximation for the antenna gain as follows [10]:

$$G(\xi, \tilde{\phi}) \simeq G_0 \exp\left\{-\frac{2}{\gamma}\sin^2\left[\theta(\xi, \tilde{\phi})\right]\right\} \quad (5)$$

with

$$\cos\left[\theta(\xi, \tilde{\phi})\right] = \frac{\cos(\xi) + \frac{\rho}{h}\sin(\xi)\cos(\tilde{\phi} - \phi)}{\sqrt{1 + \frac{\rho^2}{h^2}}} \quad (6)$$

and $\xi$ and $\tilde{\phi}$ denote mispointing angles with respect to the $z$- and $x$-axes, respectively (see Fig. 1), $G_0$ is the antenna power gain at boresight, $\gamma = (1/2\ln 2)\sin^2\theta_{3\,\text{dB}}$ is an antenna beam width parameter, and $\theta_{3\,\text{dB}}$ is the half-power antenna beam width. Note that the Cryosat-2 altimeter has an elliptical antenna that could be considered as shown in [32], which studied the FSIR in CA. However, we considered in this paper a circular antenna for simplicity (the generalization can be done at the price of a possible significant increase in model complexity). The following result is obtained (see the Appendix):

$$\text{FSIR}(t, n) = \frac{P_u}{2\pi}\left(1 + \frac{ct}{2h}\right)^{-3} U(t)$$
$$\times\left\{\int_{D_{t,n}} \exp\left\{f\left[\tilde{\phi} - \phi, \epsilon(t), \xi\right]\right\} d\phi\right\} \quad (7)$$

where $U(.)$ is the Heaviside function, and

$$f\left[\tilde{\phi} - \phi, \epsilon(t), \xi\right] = -\frac{4}{\gamma}\left[1 - \frac{\cos^2(\xi)}{1 + \epsilon^2(t)}\right]$$
$$+ b(t, \xi) + a(t, \xi)\cos(\tilde{\phi} - \phi) - b(t, \xi)\sin^2(\tilde{\phi} - \phi) \quad (8)$$

with

$$\epsilon^2(t) = \left(\frac{\rho}{h}\right)^2 \simeq \frac{ct}{h}$$
$$P_u = \frac{\lambda^2 G_0^2 c\sigma^0}{4(4\pi)^2 L_p h^3}$$
$$a(t, \xi) = \frac{4\epsilon(t)}{\gamma}\frac{\sin(2\xi)}{1 + \epsilon^2(t)}$$

$$b(t, \xi) = \frac{4\epsilon^2(t)}{\gamma}\frac{\sin^2(\xi)}{1 + \epsilon^2(t)}$$

$$\phi_{t,n} = \text{Re}\left[\arctan\left(\frac{y_n}{\sqrt{\rho^2(t) - y_n^2}}\right)\right] = \pi - \phi'_{t,n+1}$$

$$\phi_{t,n+1} = \text{Re}\left[\arctan\left(\frac{y_{n+1}}{\sqrt{\rho^2(t) - y_{n+1}^2}}\right)\right] = \pi - \phi'_{t,n}$$

$$y_n = \frac{h\lambda}{2v_s}f_n. \quad (9)$$

In the given notations, $f_n = (n - (NN_f/2) - 0.5)(F/N_f)$, with $n \in \{1, \ldots, NN_f\}$, is the $n$th Doppler frequency,[2] $N = 64$ is the number of pulses per burst, $N_f$ is the frequency oversampling factor, $y_n$ is the coordinate of the $n$th along-track beam, $v_s$ is the satellite velocity, and $\text{Re}(x)$ denotes the real part of the complex number $x$. In [22], an analytical expression of $\text{FSIR}(t, n)$ was derived by considering the case of an antenna without the mispointing angle, i.e., $\xi = 0$. In this paper, the case of a nonzero mispointing angle $\xi$ is taken into consideration.

A change of variables $u = \tilde{\phi} - \phi$ in (7) leads to

$$\text{FSIR}(t, n) = \frac{P_u}{2\pi}\left(1 + \frac{ct}{2h}\right)^{-3} U(t)$$
$$\times \exp\left\{-\frac{4}{\gamma}\left[1 - \frac{\cos^2(\xi)}{1 + \epsilon^2(t)}\right] + b(t, \xi)\right\}$$
$$\times\left[Q(\tilde{\phi} - \phi_{t,n+1}, \tilde{\phi} - \phi_{t,n})\right.$$
$$\left. + Q\left(\tilde{\phi} - \phi'_{t,n+1}, \tilde{\phi} - \phi'_{t,n}\right)\right] \quad (10)$$

with

$$Q(u_1, u_2) = \exp\left(-\frac{b}{2}\right)\int_{u_1}^{u_2}\exp\left[a\cos(u) + \frac{b}{2}\cos(2u)\right] du \quad (11)$$

where the parameters $(t, \xi)$ in $a$ and $b$ are omitted for brevity. Using the results in [33, p. 376; see eq. (9.6.34)], the following expressions are obtained:

$$\exp\left[a\cos(u)\right] = I_0(a) + 2\sum_{k=1}^{\infty} I_k(a)\cos(ku) \quad (12)$$

$$\exp\left[\frac{b}{2}\cos(2u)\right] = I_0\left(\frac{b}{2}\right) + 2\sum_{k=1}^{\infty} I_k\left(\frac{b}{2}\right)\cos(2ku) \quad (13)$$

where $I_k$ is the $k$th order modified Bessel function of the first kind.

*1) First Approximation:* The infinite sum of Bessel functions appearing in (13) can be reduced to

$$\exp\left[\frac{b}{2}\cos(2u)\right] \simeq I_0\left(\frac{b}{2}\right) \quad (14)$$

with a small loss of accuracy because of the very small values of the positive variable $b$. Indeed, the zero-order Bessel function is sufficient to approximate this sum since the maximum value of $b(t, \xi)$ (considering a pessimistic case $\xi = 1$ degree) is less

[2]We considered the case of $N = 64$ Doppler beams that results from the emission of 64 pulses per burst.

than $8 \times 10^{-4}$. The error associated with this value of $b$ is upper bounded as follows:

$$\forall u, \quad \left| \exp\left[\frac{b}{2}\cos(2u)\right] - I_0\left(\frac{b}{2}\right) \right|$$
$$\leq \left| \exp\left(\frac{b}{2}\right) - I_0\left(\frac{b}{2}\right) \right| = 4 \times 10^{-4} \quad (15)$$

which is a negligible error since it represents 0.04% of $\exp(b/2)$ (this approximation will be further justified in the rest of this paper). By using (12)–(14), we obtain the approximation $\mathrm{FSIR}(t,n) \simeq \mathrm{FSIR}_1(t,n)$, where

$$\mathrm{FSIR}_1(t,n) = \frac{P_u}{\pi}\left(1 + \frac{ct}{2h}\right)^{-3} U(t)$$
$$\times \exp\left[-\frac{4}{\gamma}\left(1 - \frac{\cos^2(\xi)}{1+\epsilon^2(t)}\right) + \frac{b}{2}\right]I_0\left(\frac{b}{2}\right)$$
$$\times \left[I_0(a)(\phi_{t,n+1} - \phi_{t,n}) + \sum_{k=1}^{\infty}\frac{1}{k}I_k(a)h_{k,n}(\tilde{\phi})\right]$$
$$(16)$$

and where

$$h_{k,n}(\tilde{\phi})$$
$$= \begin{cases} 2\cos(k\tilde{\phi})\left[\sin(k\phi_{t,n+1}) - \sin(k\phi_{t,n})\right], & \text{for even } k \\ -2\sin(k\tilde{\phi})\left[\cos(k\phi_{t,n+1}) - \cos(k\phi_{t,n})\right], & \text{for odd } k. \end{cases}$$
$$(17)$$

*2) Second Approximation:* The infinite sum in (16) can be truncated by keeping a finite number $m$ of elements according to the desired precision. The resulting FSIR, including the mispointing angles $\xi$ and $\tilde{\phi}$, can be finally approximated as $\mathrm{FSIR}(t,n) \simeq \mathrm{FSIR}_2(t,n)$, where

$$\mathrm{FSIR}_2(t,n) = \frac{P_u}{\pi}\left(1 + \frac{ct}{2h}\right)^{-3} U(t)$$
$$\times \exp\left[-\frac{4}{\gamma}\left(1 - \frac{\cos^2(\xi)}{1+\epsilon^2(t)}\right) + \frac{b}{2}\right]I_0\left(\frac{b}{2}\right)$$
$$\times \left[I_0(a)(\phi_{t,n+1} - \phi_{t,n}) + \sum_{k=1}^{m}\frac{1}{k}I_k(a)h_{k,n}(\tilde{\phi})\right]$$
$$(18)$$

where $[1 + (ct/2h)]^{-3}$ might be approximated by 1 as in [10]. Note that the proposed model (18) reduces to the model in [22] for $\xi = 0°$ (absence of mispointing angle) since $a(t,\xi = 0) = b(t,\xi = 0) = 0$. Finally, the Earth curvature can be introduced by dividing the time $t$ in (18) by the curvature factor $\alpha = 1 + (h/R) = 1.11$, where $R = 6378137$ m is the Earth radius [22], [26], [34].

### C. Multilook Model

The reflected power $P(t,f)$ associated with a DDM is obtained by a numerical computation of the double convolution (1), where $\mathrm{FSIR}(t,f)$ is approximated by the analytical expression (18), and $\mathrm{PDF}(t)$ and $\mathrm{PTR}(t,f)$ are given in (2).[3] This

[3]Note that the proposed model allows the use of other models for PDF and PTR. For instance, a PDF including the skewness could be used to better represent the distribution of the heights of the specular scatterers. Moreover, a measured PTR could also be used instead of (2).
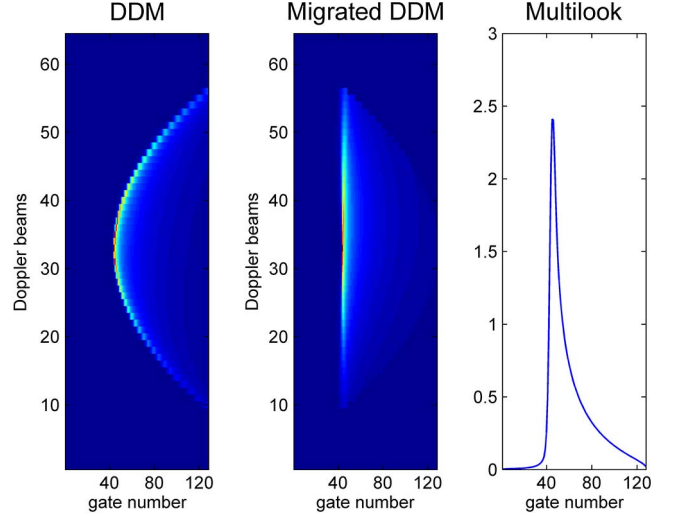


Fig. 3. Construction of a multilook waveform. (Left) A delay/Doppler map (DDM), (Middle) DDM after range migration, and (Right) multilook echo.

convolution has to be computed after applying appropriate time and frequency oversampling, a time shift by epoch $\tau$, and an undersampling as in [22]. The multilook model is formed by summing the migrated Doppler beams as follows (see [1], [3], and [22] for more details about range migration):

$$s(t) = \sum_{n=1}^{N} P_2(t - \delta t_n, f_n) \quad (19)$$

where $P_2(t,f) = \mathrm{FSIR}_2(t,f) * \mathrm{PDF}(t) * \mathrm{PTR}(t,f)$, and $\delta t_n \simeq \alpha(h\lambda^2/4cv_s^2)f_n^2$ is the delay compensation expressed in seconds. Note that each ground Doppler beam is observed by $N_p > N$ pulses resulting in $N_p$ signals. However, we consider in this paper that we obtain only $N = 64$ different signal shapes while the other observations will only reduce the noise level (i.e., the shape of successive signals is almost the same). Note also that the resulting model (19) is parameterized by the parameter vector $\boldsymbol{\theta} = (\mathrm{SWH}, P_u, \tau, \xi_{\mathrm{ac}}, \xi_{\mathrm{al}})^T$, where $\xi_{\mathrm{ac}}$ and $\xi_{\mathrm{al}}$ are the across-track (i.e., roll angle) and along-track (i.e., pitch angle) mispointing angles defined as

$$\xi_{\mathrm{al}} = \xi\sin(\tilde{\phi}) \text{ and } \xi_{\mathrm{ac}} = \xi\cos(\tilde{\phi}). \quad (20)$$

An example of reflected power $P_2(t,f)$, obtained with the model (18) for $\mathrm{FSIR}_2(t,f)$, is displayed in Fig. 3 (left) for 64 Doppler beams, 128 samples (or so called "gates"), the altimetric parameters $P_u = 1$, SWH $= 1$ m, $\tau = 44$ gates, $\xi_{\mathrm{al}} = \xi_{\mathrm{ac}} = 0.1°$ and other parameters (valid for the rest of this paper) summarized in Table I. This figure shows an ellipsoidal shape of the waveform resulting from the increasing slant range when going away from the central nadir beam. Fig. 3 (middle) shows an example of a DDM obtained after range migration, whereas Fig. 3 (right) shows the resulting multilook echo obtained after summing the contributions of the migrated Doppler beams. Note finally that the discrete multilook echo is gathered in the vector $\boldsymbol{s} = (s_1, \ldots, s_K)^T$, where $K = 128$ gates and $s_k = s(kT)$.

TABLE I
SIMULATION PARAMETERS

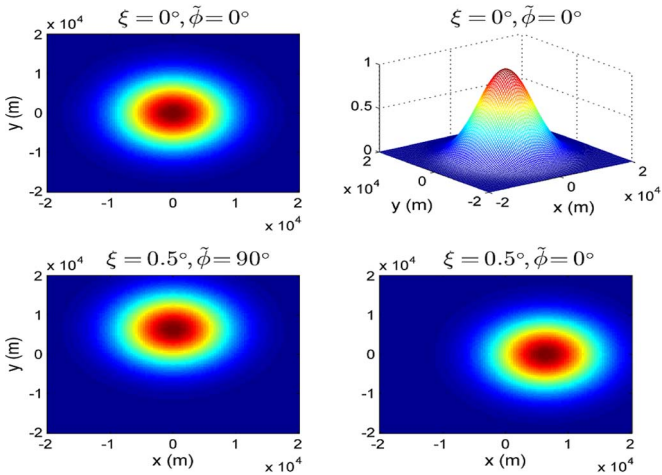| Parameter | Value |
|---|---|
| Frequency | 13.575 GHz |
| Wavelength ($\lambda$) | 2.21 cm |
| Bandwidth (B) | 320 MHz |
| Altitude (h) | 730 km |
| Burst repetition frequency (BRF) | 85 Hz |
| Pulse repetition frequency (PRF) | 18182 Hz |
| 3 dB Antenna beam width ($\theta_{3\text{dB}}$) | 1.1388 degrees |
| Velocity ($v_s$) | 7000 m/s |
| Pulses per burst | 64 pulses |
| Burst length ($\tau_b$) | 3.5 ms |
| Doppler beam width | 327 m |



Fig. 4. Antenna gain with different mispointing angles.

## D. Analysis of FSIR Versus Mispointing Angles

Antenna mispointing is introduced by means of two variables $\xi$ and $\tilde{\phi}$, which are directly related to the along- and across-track mispointing angles, as shown in (20). It is interesting to analyze the effects of these two variables on the resulting echo. The proposed model sums the energy backscattered by the sea surface to yield a 2-D flat surface impulse response FSIR$(t, f)$. The temporal dimension is introduced by the propagation circles where each time instant is related to a circle of radius $\rho(t) = \sqrt{hct}$, whereas the frequential dimension is introduced by the rectangular Doppler beams [22]. While this mapping remains constant with respect to the mispointing angles, the backscattered energy depends on $\xi$ and $\tilde{\phi}$ via the antenna gain in (5). Fig. 4 illustrates the behavior of the antenna gain for different values of mispointing angles. In the absence of mispointing, the maximum of the antenna gain occurs at $x = y = 0$. However, the along-track mispointing (see Fig. 4, bottom left) moves the maximum along the $y$-axis, whereas the across-track mispointing (see Fig. 4, bottom right) moves it along the $x$-axis, as expected. This behavior of the antenna gain induces different effects on the corresponding multilook echo. Consider first the along-track mispointing. Fig. 5 shows the noiseless DDM[4] obtained with $\xi_{\text{al}} = 0.5°$ and $\xi_{\text{ac}} = 0°$. This figure shows an energy migration from the lower Doppler

[4]The waveforms shown in Figs. 5–8 are noiseless. The objective of these figures is to highlight the behavior of the delay/Doppler echo as a function of mispointing angles.
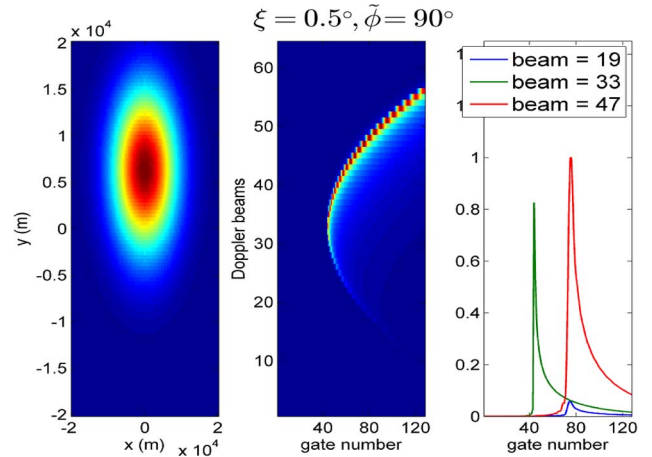


Fig. 5. Antenna gain, DDM, and Doppler echoes representation for an along-track mispointing angle and $\xi_{\text{al}} = 0.5°$ (with $\xi_{\text{ac}} = 0°$).



Fig. 6. Effect of along-track mispointing on (top) the multilook echoes and (bottom) the normalized multilook echoes (obtained with $P_u = 1$, $\tau = 44$ gates, SWH = 3 m, and $\xi_{\text{ac}} = 0°$).



Fig. 7. Antenna gain, DDM, and Doppler echoes representation for an across-track mispointing angle $\xi_{\text{ac}} = 0.5°$ (with $\xi_{\text{al}} = 0°$).

beams to the higher Doppler beams (because of the move of the antenna gain along the $y$-axis). This along-track mispointing reduces the amplitude of the multilook echo as shown in Fig. 6 (top), whereas it does not change the shape of the waveform as shown in Fig. 6 (bottom) representing normalized waveforms. Fig. 7 shows the DDM obtained with an across-track mispointing angle $\xi_{\text{ac}} = 0.5°$ and $\xi_{\text{al}} = 0°$. This figure shows an
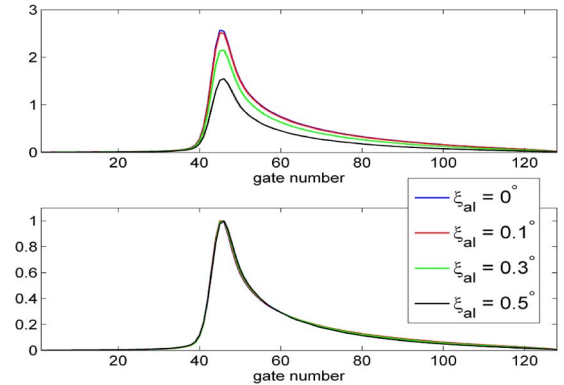
Fig. 8. Effect of across-track mispointing on (top) the multilook echoes and (bottom) the normalized multilook echoes (obtained with $P_u = 1$, $\tau = 44$ gates, SWH = 3 m, and $\xi_{\mathrm{al}} = 0°$).
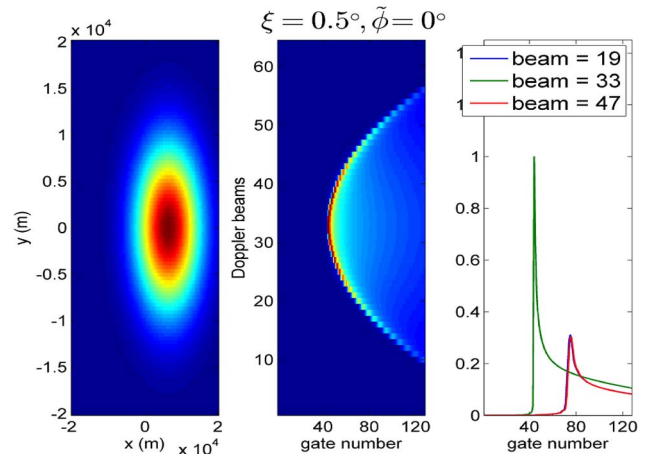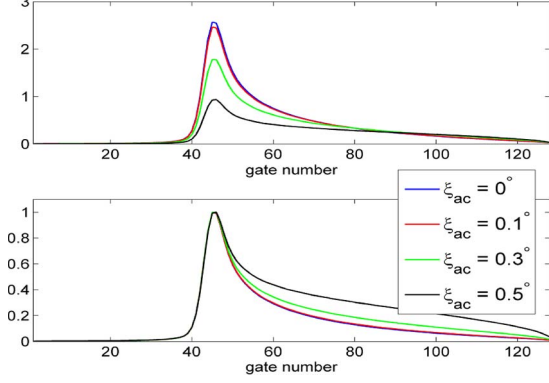
energy migration from the low time gates to the high time gates (because of the move of the antenna gain in the $x$-axis). This across-track mispointing reduces the amplitude of the multilook echo as shown in Fig. 8 (top), but it also affects the shape of the waveform as shown in Fig. 8 (bottom) representing normalized waveforms. These results are in agreement with those obtained in the SAMOSA (synthetic aperture radar altimetry mode studies and applications) project [35], for example. Note finally that the obtained results show that the shape of the multilook echo depends on the parameter vector (SWH, $\tau$, $P_u$, $\xi_{\mathrm{ac}}$) while $\xi_{\mathrm{al}}$ mainly affects the amplitude of the waveform. Therefore, we will be interested in estimating these four parameters when considering $\xi_{\mathrm{al}} = 0°$ in the following.

## III. PARAMETER ESTIMATION

This section investigates the different methods for estimating the parameters of the multilook echo (19) from noisy measurement. The LS procedure considered for this estimation is presented in Section III-A, whereas the criteria used for performance evaluation are reported in Section III-B.

### A. Estimation Algorithm

The considered LS estimator is defined as

$$\hat{\boldsymbol{\theta}}_{\mathrm{LS}} = \arg\min_{\boldsymbol{\theta}} \frac{1}{2} \sum_{k=1}^{K} g_k^2(\boldsymbol{\theta}) \qquad (21)$$

where $g_k(\boldsymbol{\theta}) = y_k - s_k(\boldsymbol{\theta})$ is the vector of residues, and $\boldsymbol{y} = (y_1, \ldots, y_K)^T$ is a noisy version of $\boldsymbol{s}(\boldsymbol{\theta}) = [s_1(\boldsymbol{\theta}), \ldots, s_K(\boldsymbol{\theta})]^T$, which depends on the parameter vector of interest $\boldsymbol{\theta}$. In this paper, we propose to solve (21) using the same numerical optimization method as in [22], i.e., by using the Levenberg–Marquardt algorithm [36]. This algorithm uses a gradient descent approach to update $\boldsymbol{\theta}$ as follows:

$$\boldsymbol{\theta}^{(i+1)} = \boldsymbol{\theta}^{(i)} - \left[ \boldsymbol{J}^T \boldsymbol{J} + \mu \boldsymbol{I}_J \right]^{-1} \boldsymbol{J}^T \boldsymbol{g}\left(\boldsymbol{\theta}^{(i)}\right) \qquad (22)$$

where $\boldsymbol{\theta}^{(i)}$ is the estimate of $\boldsymbol{\theta}$ at the $i$th iteration, $\boldsymbol{J} = \boldsymbol{J}(\boldsymbol{\theta}^{(i)}) = \left[ \frac{\partial \boldsymbol{g}(\boldsymbol{\theta}^{(i)})}{\partial \theta_1}, \ldots, \frac{\partial \boldsymbol{g}(\boldsymbol{\theta}^{(i)})}{\partial \theta_J} \right]$ is a $K \times J$ matrix such that $\frac{\partial \boldsymbol{g}(\boldsymbol{\theta})}{\partial \theta_j} =$

$\left[ \frac{\partial g_1(\boldsymbol{\theta})}{\partial \theta_j}, \ldots, \frac{\partial g_K(\boldsymbol{\theta})}{\partial \theta_j} \right]^T$, $J$ is the number of parameters to estimate, $\boldsymbol{I}_J$ is the $J \times J$ identity matrix, and $\mu$ is a regularization parameter. The application of the recursive parameter update (22) requires to compute the derivatives of the residues $\frac{\partial \boldsymbol{g}(\boldsymbol{\theta})}{\partial \theta_j}$. In this paper, we propose to compute these derivatives numerically as follows:

$$\frac{\partial \boldsymbol{g}(\boldsymbol{\theta})}{\partial \theta_j} = -\frac{\partial \boldsymbol{s}(\boldsymbol{\theta})}{\partial \theta_j} \simeq -\frac{\boldsymbol{s}(\theta_j + \Delta\theta_j) - \boldsymbol{s}(\theta_j)}{\Delta\theta_j}. \qquad (23)$$

### B. Estimation Performance

For synthetic waveforms, we propose to evaluate the estimation performance of the LS estimator by considering its root-mean-square error (RMSE), bias (Bias), and standard-deviation (STD) defined as

$$\mathrm{RMSE}\,(\theta_i) = \sqrt{\frac{1}{N_{\mathrm{MC}}} \sum_{j=1}^{N_{\mathrm{MC}}} \left[ \theta_i - \hat{\theta}_i(j) \right]^2} \qquad (24)$$

$$\mathrm{Bias}\,(\theta_i) = \frac{1}{N_{\mathrm{MC}}} \sum_{j=1}^{N_{\mathrm{MC}}} \hat{\theta}_i(j) - \theta_i = \overline{\theta}_i - \theta_i \qquad (25)$$

$$\mathrm{STD}\,(\theta_i) = \sqrt{\frac{1}{N_{\mathrm{MC}}} \sum_{j=1}^{N_{\mathrm{MC}}} \left[ \hat{\theta}_i(j) - \overline{\theta}_i \right]^2}, \quad i = 1, \ldots, J \qquad (26)$$

where $\theta_i$ is the true parameter, $\hat{\theta}_i(j)$ is the estimated parameter for the $j$th waveform, and $N_{\mathrm{MC}}$ is the number of simulated waveforms (generated with the same value of $\theta_i$ but with different noise realizations).

For real Cryosat-2 waveforms, the estimated parameters will be compared with those obtained with the model in [22] to show the potential gain obtained with a model accounting for the antenna mispointing. The normalized reconstruction error (NRE) defined by

$$\mathrm{NRE}(j) = \sqrt{\frac{\sum_{k=1}^{K} \left[ y_k(j) - s_k(\boldsymbol{\theta}_j) \right]^2}{\sum_{k=1}^{K} y_k^2(j)}} \qquad (27)$$

will also be used to evaluate the quality of the fit between the $j$th real echo $\boldsymbol{y}(j)$ and the proposed model. Note finally that the averaged NRE (ANRE) is also used when considering $N_{\mathrm{MC}}$ real echoes, i.e.,

$$\mathrm{ANRE} = \frac{1}{N_{\mathrm{MC}}} \sum_{j=1}^{N_{\mathrm{MC}}} \mathrm{NRE}(j). \qquad (28)$$

## IV. SIMULATION AND IN-ORBIT RESULTS

This section presents simulation results obtained with the proposed model. The approximations used to obtain the analytical FSIR are first justified. The quality of the proposed model and the corresponding estimation algorithms is then evaluated by considering simulated and real Cryosat-2 waveforms.

### A. Justification of the FSIR Approximations

This section validates model (18) by comparison with an "exact model" resulting from a numerical computation of
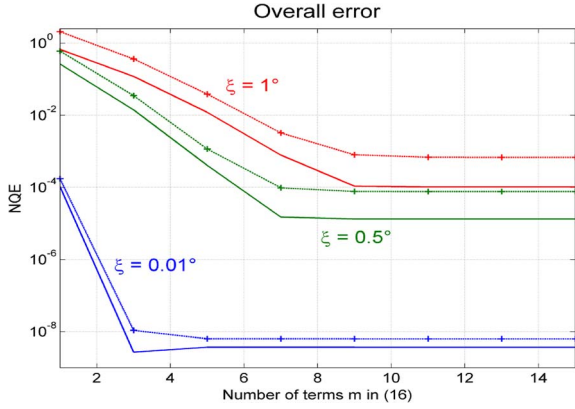
Fig. 9. Overall error versus $m$ (for different mispointing angles). Global NQE (continuous line) and maximum NQE (crossed line) for $\xi = 0.01°$ (in blue), $\xi = 0.5°$ (in green), and $\xi = 1°$ (in red).

integral (10). This validation is conducted by analyzing the errors introduced by the two successive approximations. The normalized quadratic error (NQE) defined by

$$\mathrm{NQE}(\boldsymbol{s}, \boldsymbol{r}) = \sqrt{\frac{\sum_{k=1}^{K}(s_k - r_k)^2}{\sum_{k=1}^{K} r_k^2}} \qquad (29)$$

is used to compare the exact multilook echo $\boldsymbol{r}$ obtained by numerically convolving the FSIR (10) with (2a) and (2b) and the approximated multilook echo $\boldsymbol{s}$ obtained using the proposed approximated FSIR (18). Note that the study of this error will allow for the fixing of the number $m$ of terms in (18).

Fig. 9 shows the global error NQE (continuous line) as a function of $m$ for different mispointing angles (the across- and along-track mispointing provide similar results). This figure also shows a theoretical upper bound for NQE (crossed line), which was derived in [30] and [37]. The interested reader is invited to consult [30] and [37] for more details about the computation of this upper bound denoted as $\mathrm{NQE}^{\mathrm{max}}$ in this paper. Note first that the global error is always below the theoretical maximum error $\mathrm{NQE}^{\mathrm{max}}$, as expected. Moreover, Fig. 9 shows that the error is an increasing function of the mispointing angles and that it decreases when the number of terms $m$ increases. This result was expected since increasing $m$ provides a better approximation of the infinite sum in (16). Note also that some simulation results have shown that the minimum NQE obtained between a noisy echo and an echo without noise is about $7 \times 10^{-2}$, which means that we have to consider a value of $m$ that provides a lower error. For the pessimistic case $\xi = 1°$, $m = 6$ is sufficient to obtain the desired error level. This value will be considered in the rest of this paper.

### B. Simulated Waveforms

*1) Generation:* To generate realistic waveforms, the multilook signal $s(t)$ of (19) is corrupted by speckle noise as in [22] and [38], resulting in a noisy echo $y(t)$ defined by

$$y(t) = \sum_{n=1}^{N} P(t - \delta t_n, f_n)\, q(t - \delta t_n, n) \qquad (30)$$

where $q(t, n)$ is a multiplicative independent and identically distributed speckle noise distributed according to a gamma distribution $\Gamma(L, 1/L)$, where $L$ is the number of bursts observing a surface beam ($L = 4$ in our simulations, which means that $N_p = LN = 256$ pulses).

The noise level can be evaluated using the equivalent number of looks (ENL) defined in [3], [38], and [39] as follows:

$$\mathrm{ENL}(k) = \frac{E^2[y_k]}{E\left\{[y_k - E(y_k)]^2\right\}} \qquad (31)$$

where $E(.)$ is the expectation operator. The ENL depends on the time instant and is equivalent to the number of independent intensities averaged in each time gate. It has a mean value close to 150 independent looks, which can be expressed in decibels as $\mathrm{SNR}_{\mathrm{dB}} = 10\log(\mathrm{ENL}) \simeq 21$ dB. The reader is invited to consult [22] and [38] for more details about speckle noise generation.

*2) Estimation Scenarios:* The proposed multilook model defined in (19) depends on five altimetric parameters contained in the unknown parameter vector $\boldsymbol{\theta}_5 = (\theta_1, \ldots, \theta_5)^T = (\mathrm{SWH}, P_u, \tau, \xi_{\mathrm{ac}}, \xi_{\mathrm{al}})^T$. There are different ways to take advantage of this model.

- Replace $\xi_{\mathrm{al}}$ and $\xi_{\mathrm{ac}}$ by known mispointing angles[5] and estimate the three remaining parameters $(\mathrm{SWH}, P_u, \tau)^T$ by the Levenberg–Marquardt algorithm. The resulting estimation strategy will be denoted as G-DDA3 (for generalized delay/Doppler altimetric model with three unknown parameters).
- Estimate the five parameters $(\mathrm{SWH}, P_u, \tau, \xi_{\mathrm{ac}}, \xi_{\mathrm{al}})^T$ by the Levenberg–Marquardt algorithm. Due to the strong correlation between $\xi_{\mathrm{al}}$ and $P_u$, we have observed that this strategy does not provide interesting results (see [30] for more details). As a consequence, we consider an alternative approach where $\xi_{\mathrm{al}}$ is set to 0, and the four remaining parameters are estimated using the Levenberg–Marquardt algorithm. This strategy will be referred to as DDA4 (for DDA with four unknown parameters) in this paper.

Of course, the estimations provided by G-DDA3 and DDA4 need to be compared with those obtained with the algorithm in [22] denoted as DDA3. It is the objective of the following section.

*3) Parameter Estimation:* This section evaluates the performance of the proposed algorithms for simulated multilook waveforms. All results presented in this section have been averaged using $N_{\mathrm{MC}} = 500$ Monte Carlo runs (with the same parameters but with different noise realizations). The first experiment considers a fixed parameter vector $(P_u, \tau, \xi_{\mathrm{ac}}, \xi_{\mathrm{al}})^T = (1, 31\ \mathrm{gates}, 0°, 0°)^T$ (corresponding to an absence of mispointing) with varying SWH. Fig. 10 shows the parameter RMSEs obtained with DDA3 and DDA4 (G-DDA3 is the same as DDA3 since $\xi_{\mathrm{ac}} = \xi_{\mathrm{al}} = 0°$). This figure shows a similar performance for DDA3 and DDA4 algorithms. Thus, there is no performance reduction when estimating the across-track mispointing angle $\xi_{\mathrm{ac}}$ in the absence of mispointing. Note that

---

[5]The Cryosat-2 satellite is able to estimate the mispointing angles $\xi_{\mathrm{al}}$ and $\xi_{\mathrm{ac}}$. Those estimates are obtained using the satellite star trackers and the same procedure as in [40].
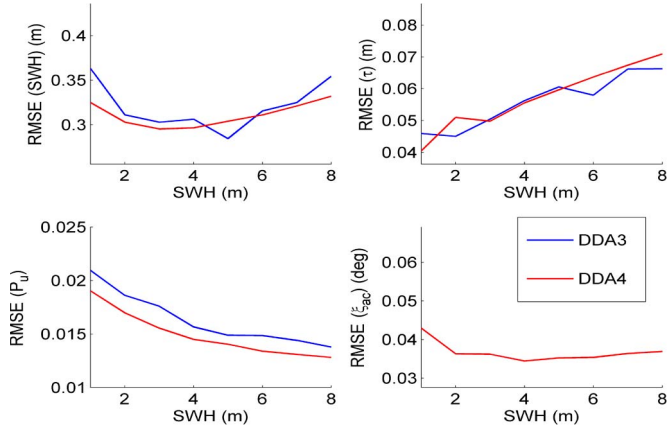
Fig. 10. Parameter RMSEs versus SWH in the absence of mispointing for DDA3 and DDA4 algorithms (500 Monte Carlo runs, $P_u = 1$, $\tau = 31$ gates, $\xi_{al} = 0°$, $\xi_{ac} = 0°$).
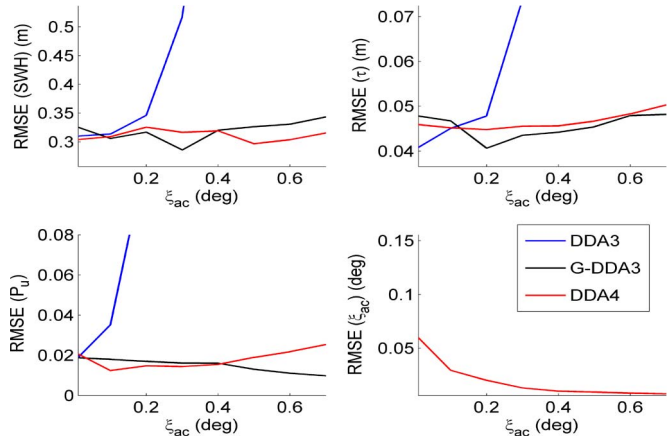


Fig. 11. Parameter RMSEs versus $\xi_{ac}$ for DDA3, G-DDA3, and DDA4 algorithms (500 Monte Carlo runs, $P_u = 1$, SWH = 2 m, $\tau = 31$ gates, $\xi_{al} = 0°$).

DDA4 also provides an estimation of $\xi_{ac}$ with a constant RMSE close to $0.035°$ for different values of SWH.

The second set of experiments evaluates the performance of the proposed algorithms for the parameter vector $(\text{SWH}, P_u, \tau, \xi_{al})^T = (2\,\text{m}, 1, 31\,\text{gates}, 0°)^T$ with varying $\xi_{ac}$. Fig. 11 shows that G-DDA3 (in which we consider the actual values of mispointing angles) and DDA4 similarly behave for the parameters SWH, $\tau$, and $P_u$ (the corresponding RMSEs belong to the same intervals [0.28, 0.34] m, [4, 5] cm, and [0.01, 0.03]). This similarity in the RMSE of SWH, $\tau$ and $P_u$ (when considering DDA4 and G-DDA3) for different values of $\xi_{ac}$, shows that the presence of across-track mispointing does not affect their estimation. Conversely, the DDA3 algorithm is more sensitive to the mispointing angle $\xi_{ac}$ and shows a bad performance for large values of this parameter (the RMSE exceeds 40 cm for SWH, 6 cm for $\tau$, and 0.08 for $P_u$ when $\xi_{ac} > 0.25°$, as shown in Fig. 11). Fig. 11 (bottom right) finally shows that $\text{RMSE}(\xi_{ac})$ is a decreasing function of $\xi_{ac}$. This property can be explained by the fact that the delay/Doppler altimetric waveform is less peaky for large values of $\xi_{ac}$ (see Fig. 8), facilitating the distinction between waveforms. To summarize, the results obtained in this section illustrate the good performance of the DDA4 algorithm for estimating the
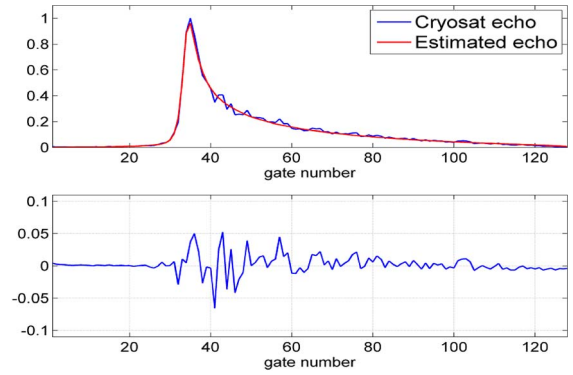


Fig. 12. Example of estimated Cryosat-2 echo using the proposed DDA4 model (NRE = 0.065). (Top) Real Cryosat-2 echo superimposed with its estimation. (Bottom) Difference between the real Cryosat-2 echo and its estimation.
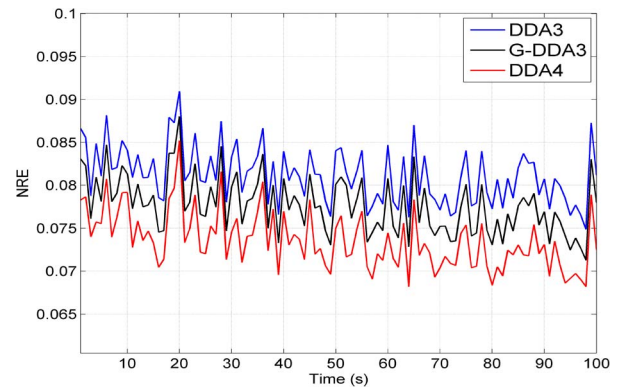


Fig. 13. NRE estimates for 100 s of Cryosat-2 data when considering DDA3, G-DDA3, and DDA4.

altimetric parameters $(\text{SWH}, P_u, \tau)$ and the mispointing angle $\xi_{ac}$ for synthetic data.

### C. CRYOSAT-2 Waveforms

This section evaluates the performance of the proposed model and algorithms for real oceanic Cryosat-2 waveforms. The considered data set lasts approximately 400 s and was obtained in May 2012 by the Cryosat processing prototype (CPP) developed by the Centre National d'Études Spatiales (CNES) [41] (which is doing level-1 processing). Note that the CNES-CPP uses data preprocessed to a full bit rate provided by the European Space Agency [42]. Fig. 12 shows an example of the estimated Cryosat-2 echo obtained with DDA4. As for DDA3 (see [22]), this figure shows an excellent fit between the two echoes and a very low difference between them.[6] The goodness of fit can be quantified by the NRE criteria introduced in Section III-B. Fig. 13 shows the obtained NREs when considering the three estimation strategies for 100 s of data. This figure allows the performance of the different algorithms to be compared. DDA4 provides the best fit between the observed echo and the proposed model, followed by G-DDA3 and DDA3. Table II summarizes the obtained ANREs when considering the different DDA strategies confirming the supe-

---

[6]More results are available in the separate technical report [30].

TABLE II
AVERAGED NRE WHEN CONSIDERING DDA3,
G-DDA3, AND DDA4 ALGORITHMS

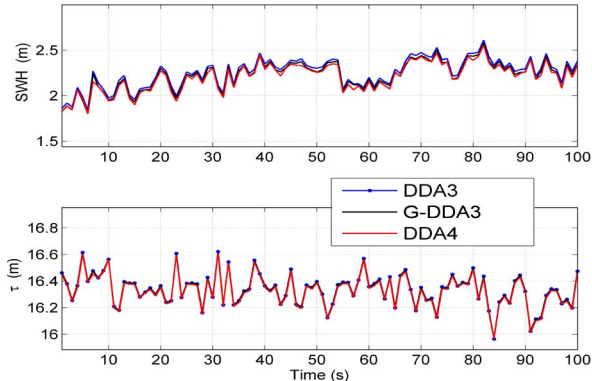| | DDA3 | G-DDA3 | DDA4 |
|---|---|---|---|
| ANRE ($\times 10^{-2}$) | 8.08 | 7.78 | 7.35 |



Fig. 14. Parameter estimates for 100 s of Cryosat-2 data when considering DDA3, G-DDA3, and DDA4. (Top) SWH. (Bottom) $\tau$.
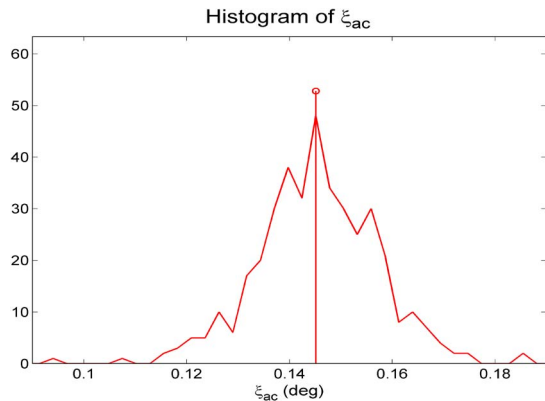


Fig. 15. Histogram of the estimated $\xi_{ac}$ (in degrees) when considering DDA4.

riority of the DDA4 algorithm. Note that this performance gain was expected since the estimation of more parameters generally leads to a better fit (provided that the criterion to optimize with additional parameters is not strongly multimodal).

Considering the estimated parameters, Fig. 14 shows a good agreement between the three estimation strategies when considering the parameters $\tau$ and SWH (for 100 s of data). Fig. 15 shows the histograms of the estimated parameter $\xi_{ac}$ when considering DDA4. This figure shows that real data present relatively small mispointing angles distributed around an estimated value of $\xi \simeq 0.146°$, which is in agreement with the results in [40], where $\xi$ is estimated around $\simeq 0.1282°$ when considering Cryosat-2 data. Table III summarizes the means and STDs obtained with the three estimation strategies. This table shows that the means of the different estimated parameters (SWH, $P_u$, $\tau$) are similar. However, interestingly, the STDs obtained with DDA4 are always smaller than those obtained with the other algorithms (see Table III), illustrating the interest of this algorithm. This result can be explained as follows. For simulated echoes, the true value of the parameters is exactly known. In this case, G-DDA3 and DDA4 present

TABLE III
MEANS AND STDs FOR DDA3, G-DDA3, AND DDA4 ALGORITHMS.
ALONG EACH STD COLUMN, THE FIRST SMALLER VALUE IS
IN GREEN, AND THE SECOND SMALLER VALUE IS IN RED

| | | $\tau$ (m) | SWH (m) | $P_u$ | $\xi_{ac}$ (deg) | $\xi_{al}$ (deg) | $\xi$ (deg) |
|---|---|---|---|---|---|---|---|
| Means | DDA3 | 16.274 | 2.289 | 90.213 | - | - | - |
| | G-DDA3 | 16.270 | 2.247 | 92.803 | 0.083 | 0.0572 | 0.109 |
| | DDA4 | 16.262 | 2.234 | 96.993 | 0.146 | - | 0.146 |
| STDs | DDA3 | 0.0843 | 0.355 | 1.933 | - | - | - |
| | G-DDA3 | 0.0845 | 0.354 | 1.987 | $1.01 \times 10^{-4}$ | $7 \times 10^{-4}$ | $4 \times 10^{-4}$ |
| (20 Hz) | DDA4 | 0.0827 | 0.351 | 1.871 | 0.031 | - | 0.031 |

similar performance, as shown in Fig. 11. As a consequence, G-DDA3 has to be preferred since it estimates less parameters, leading to a reduced computational time. However, when considering Cryosat-2 echoes, the values of the mispointing angles are only approximately known. In this case, DDA4 performs better than G-DDA3 run with the approximated angles provided by Cryosat-2. The obtained results show that DDA4 allows the variability of the mispointing angles with respect to the estimated angles provided by the star trackers to be mitigated when compared with G-DDA3.

## V. CONCLUSION

This paper has defined a generalized semi-analytical model for delay/Doppler altimetry, taking into account the effect of antenna mispointing. This model is based on a closed-form approximation of the flat surface impulse response derived under the assumption of a circular antenna pattern, no vertical speed effect, and uniform scattering. The approximations used to elaborate the proposed analytical formula for the flat surface impulse response were studied and quantified. The proposed model showed that the across-track mispointing angle affects the shape and the amplitude of the altimetric echo, whereas the along-track mispointing angle mainly affects the amplitude of the echo. There are different ways of exploiting the proposed model. Two different least squares estimation algorithms were investigated depending on the knowledge or the absence of knowledge about mispointing angles. Both algorithms provided promising results. Future work includes the consideration of the vertical speed effect and the thermal noise in the proposed model. It also includes the generalization of the proposed model by considering an elliptical antenna, as studied in [32], for the case of conventional altimetry. Considering other estimation strategies such as the maximum-likelihood estimator is also an interesting issue.

## APPENDIX
### INTEGRAL WITH RESPECT TO $\rho$ FOR THE FSIR

This section presents more details about the computation of the integral with respect to $\rho$ to obtain the FSIR in (7). Using $r = h\sqrt{1 + \epsilon^2}$, (4), and (5), we obtain

$$\text{FSIR}(t', n) = \frac{\lambda^2 \sigma^0 G_0^2}{(4\pi)^3 L_p h^4}$$

$$\times \int_{\mathbb{R}^+ \times D_{t,n}} \frac{\delta\left(t' - \frac{2r}{c}\right) \exp\left\{-\frac{4}{\gamma} \sin^2\left[\theta(\xi, \tilde{\phi})\right]\right\}}{(1 + \epsilon^2)^2} \rho d\rho d\phi \quad (32)$$

where

$$\sin^2(\theta) = \left[1 - \frac{\cos^2(\xi)}{1+\epsilon^2}\right] - \frac{\epsilon^2 \sin^2(\xi)}{1+\epsilon^2} - \frac{\epsilon \sin(2\xi)}{1+\epsilon^2} \cos(\tilde{\phi} - \phi)$$

$$+ \frac{\epsilon^2 \sin^2(\xi)}{1+\epsilon^2} \sin^2(\tilde{\phi} - \phi). \quad (33)$$

Using the change of variable $x = (2h/c)\sqrt{1+\epsilon^2}$ and the property of the Dirac distribution $h(t') = \int_{c_1}^{+\infty} \delta(x - t')h(x)dx$ for $t' \geq c_1$, where $c_1 \in \mathbb{R}^+$, integrating with respect to $x$ leads to

$$\text{FSIR}(t', n) = \frac{\lambda^2 G_0^2 c\sigma^0}{2(4\pi)^3 L_p h^3} \left(\frac{ct'}{2h}\right)^{-3} U\left(t' - \frac{2h}{c}\right)$$

$$\times \int_{D_{t,n}} \exp\left\{ f\left[\tilde{\phi} - \phi, \epsilon(t'), \xi\right]\right\} d\phi. \quad (34)$$

Note finally that (34) reduces to (7) by replacing $t'$ by its expression as a function of $t$, i.e., $t' = t + (2h/c)$.

### REFERENCES

[1] R. K. Raney, "The delay/Doppler radar altimeter," *IEEE Trans. Geosci. Remote Sens.*, vol. 36, no. 5, pp. 1578–1588, Sep. 1998.

[2] J. Jensen and R. Raney, "Delay/Doppler radar altimeter: Better measurement precision," in *Proc. IEEE IGARSS*, Seattle, WA, USA, Jul. 6–10, 1998, pp. 2011–2013.

[3] D. Wingham, L. Phalippou, C. Mavrocordatos, and D. Wallis, "The mean echo and echo cross product from a beamforming interferometric altimeter and their application to elevation measurement," *IEEE Trans. Geosci. Remote Sens.*, vol. 42, no. 10, pp. 2305–2323, Oct. 2004.

[4] L. Phalippou and V. Enjolras, "Re-tracking of SAR altimeter ocean power-waveforms and related accuracies of the retrieved sea surface height, significant wave height and wind speed," in *Proc. IEEE IGARSS*, Barcelona, Spain, Jul. 23–27, 2007, pp. 3533–3536.

[5] C. Martin-Puig *et al.*, "Theoretical model of SAR altimeter over water surfaces," in *Proc. IEEE IGARSS*, Boston, MA, USA, Jul. 7–11, 2008, pp. 242–245.

[6] L. Cutrona, W. E. Vivian, E. Leith, and G. O. Hall, "A high-resolution radar combat-surveillance system," *IRE Trans. Mil. Electron.*, vol. 5, no. 2, pp. 127–131, Apr. 1961.

[7] T. Shapiro, S. H. Zisk, A. E. E. Roge, M. A. Slade, and T. W. Tho, "Lunar topography: Global determination by radar," *Science*, vol. 178, no. 4064, pp. 939–945, Dec. 1972.

[8] H. Griffiths, "Synthetic aperture processing for full-deramp radar altimeters," *Electron. Lett.*, vol. 24, no. 7, pp. 371–373, Mar. 1988.

[9] B. Purseyyed and H. Griffiths, "A synthetic aperture altimeter," in *Proc. IEEE IGARSS*, Edinburgh, U.K., Sep. 12–16, 1988, vol. 2, pp. 981–982.

[10] G. Brown, "The average impulse response of a rough surface and its applications," *IEEE Trans. Antennas Propag.*, vol. AP-25, no. 1, pp. 67–74, Jan. 1977.

[11] G. Hayne, "Radar altimeter mean return waveforms from near-normal-incidence ocean surface scattering," *IEEE Trans. Antennas Propag.*, vol. AP-28, no. 5, pp. 687–692, Sep. 1980.

[12] E. Rodriguez, "Altimetry for non-Gaussian oceans: Height biases and estimation of parameters," *J. Geophys. Res.*, vol. 93, no. C11, pp. 14 107–14 120, Nov. 1988.

[13] L. Amarouche *et al.*, "Improving the Jason-1 ground retracking to better account for attitude effects," *Mar. Geod.*, vol. 27, no. 1/2, pp. 171–197, Aug. 2004.

[14] J. Gómez-Enri *et al.*, "Modeling ENVISAT RA-2 waveforms in the coastal zone: Case study of calm water contamination," *IEEE Geosci. Remote Sens. Lett.*, vol. 7, no. 3, pp. 474–478, Jul. 2010.

[15] A. Halimi, C. Mailhes, J.-Y. Tourneret, and P. Thibaut, "A new model for peaky altimetric waveforms," in *Proc. IEEE IGARSS*, Vancouver, BC, Canada, Jul. 24–29, 2011, pp. 2825–2828.

[16] A. Halimi, C. Mailhes, J.-Y. Tourneret, P. Thibaut, and F. Boy, "Parameter estimation for peaky altimetric waveforms," *IEEE Trans. Geosci. Remote Sens.*, vol. 51, no. 3, pp. 1568–1577, Mar. 2013.

[17] C. Gommenginger *et al.*, "Retracking altimeter waveforms near the coasts," in *Coastal Altimetry*, S. Vignudelli, A. G. Kostianoy, P. Cipollini, and J. Benveniste, Eds. Berlin, Germany: Springer-Verlag, 2011, pp. 61–101.

[18] C. Martin-Puig and G. Ruffini, "SAR altimeter retracker performance bound over water surfaces," in *Proc. IEEE IGARSS*, Cape Town, South Africa, Jul. 12–17, 2009, pp. 449–452.

[19] L. Phalippou and F. Demeestere, "Optimal re-tracking of SAR altimeter echoes over open ocean: From theory to results for SIRAL2," in *Proc. OSTST Meet.*, San Diego, CA, USA, Oct. 19–21, 2011, pp. 1–18. [Online]. Available: http://www.aviso.oceanobs.com/fileadmin/documents/OSTST/2011/oral/01_Wednesday/Splinter%201%20IP/02%20OSTST-2011-Phalippou-Demeestere.pdf

[20] A. Halimi, C. Mailhes, J.-Y. Tourneret, P. Thibaut, and F. Boy, Technical report associated with the paper "A Semi-Analytical Model for Delay/Doppler Altimetry and its Estimation Algorithm," Univ. Toulouse-CLS-CNES, Toulouse, France, Tech. Rep. [Online]. Available: http://halimi.perso.enseeiht.fr/Publications/Journals/HALIMI_TechRep_TGRS_2013_DDA3.pdf

[21] C. Martin-Puig *et al.*, "SAR altimetry over water surfaces," presented at the Oceans From Space, Venice, Italy, Apr. 2010.

[22] A. Halimi, C. Mailhes, J.-Y. Tourneret, P. Thibaut, and F. Boy, "A semi-analytical model for delay/Doppler altimetry and its estimation algorithm," *IEEE Trans. Geosci. Remote Sens.*, vol. 57, no. 7, pp. 4248–4258, Jul. 2014.

[23] Y. Shuang-Bao, L. He-Guang, X. Ke, and X. Xi-Yu, "The mean echo model and data process of SAR altimeter," in *Proc. IEEE IGARSS*, Vancouver, BC, Canada, Jul. 24–29, 2011, pp. 2077–2080.

[24] E. Rodriguez and J.-M. Martin, "Assessment of the TOPEX altimeter performance using waveform retracking," *J. Geophys. Res.*, vol. 99, no. C12, pp. 24 957–24 969, Dec. 1994.

[25] O. Z. Zanifé *et al.*, "Assesment of the JASON-1 look-up tables using multiple Gaussian functions as an approximation of the PTR," in *Proc. OSTST Meet.*, Venice, Italy, Mar. 16–18, 2006, pp. 1–17. [Online]. Available: http://www.aviso.oceanobs.com/fileadmin/documents/OSTST/2006/zanife.pdf

[26] D. B. Chelton, "Pulse compression and sea level tracking in satellite altimetry," *J. Atmos. Ocean. Technol.*, vol. 6, no. 3, pp. 407–438, Jun. 1989.

[27] R. K. Raney and L. Phalippou, "The future of coastal altimetry," in *Coastal Altimetry*, S. Vignudelli, A. G. Kostianoy, P. Cipollini, and J. Benveniste, Eds. Berlin, Germany: Springer-Verlag, 2011, pp. 61–101.

[28] S. Maus, C. M. Green, and J. D. Fairhead, "Improved ocean-geoid resolution from retracked ERS-1 satellite altimeter waveforms," *Geophys. J. Int.*, vol. 134, no. 1, pp. 243–253, Feb. 1998.

[29] D. T. Sandwell and W. H. F. Smith, "Retracking ERS-1 altimeter waveforms for optimal gravity field recovery," *Geophys. J. Int.*, vol. 163, no. 1, pp. 79–89, Oct. 2005.

[30] A. Halimi, C. Mailhes, J.-Y. Tourneret, T. Moreau, and F. Boy, Technical report associated with the paper "Including Antenna Mispointing in a Semi-Analytical Model for Delay/Doppler Altimetry", Univ. Toulouse-CLS-CNES, Toulouse, France, Tech. Rep. [Online]. Available: http://halimi.perso.enseeiht.fr/Publications/Submitted_papers/HALIMI_TechRep_TGRS_2013_DDA4.pdf

[31] J. Tournadre, B. Chapron, and N. Reul, "High-resolution imaging of the ocean surface backscatter by inversion of altimeter waveforms," *J. Atmos. Ocean. Technol.*, vol. 28, no. 8, pp. 1050–1062, Aug. 2011.

[32] D. J. Wingham and D. W. Wallis, "The rough surface impulse response of a pulse-limited altimeter with an elliptical antenna pattern," *IEEE Antennas Wireless Propag. Lett.*, vol. 9, pp. 232–235, Sep. 2010.

[33] M. Abramowitz and I. A. Stegun, *Handbook of Mathematical Functions With Formulas, Graphs, and Mathematical Tables*. New York, NY, USA: Dover, 1965.

[34] J. MacArthur, "Design of the Seasat-A radar altimeter," in *Proc. OCEANS*, Washington, DC, USA, Sep. 13–15, 1976, pp. 222–229.

[35] C. Gommenginger *et al.*, "Improved altimetric accuracy of SAR altimeters over the ocean: Observational evidence from Cryosat-2 SAR and Jason-2," in *Proc. OSTST Meet.*, San Diego, CA, USA, Oct. 19–21, 2011, pp. 1–35. [Online]. Available: http://www.aviso.oceanobs.com/fileadmin/documents/OSTST/2011/oral/01_Wednesday/Splinter%201%20IP/01%20Gommenginger%20SAMOSA_OSTST_Oct2011.pdf

[36] D. P. Bertsekas, *Nonlinear Programming*. Belmont, MA, USA: Athena Scientific, 1995.

[37] A. Halimi, "From conventional to delay/Doppler altimetry," Ph.D. dissertation, Inst. Nat. Polytech. Toulouse, Toulouse, France, 2013.

[38] A. Halimi, C. Mailhes, and J.-Y. Tourneret, "Cramér–Rao bounds and estimation algorithms for delay/Doppler and conventional altimetry," in *Proc. EUSIPCO*, Marrakech, Marocco, Sep. 9–13, 2013, pp. 1–5.

[39] C. Oliver and S. Quegan, *Understanding Synthetic Aperture Radar Images*. Reading, MA, USA: Artech House, 1998.

[40] W. H. F. Smith and R. Scharroo, "Retracking range, SWH, sigma-naught, and attitude in Cryosat conventional ocean data," in *Proc. OSTST Meet.*, San Diego, CA, USA, Oct. 19–21, 2011, pp. 1–27. [Online]. Available: http://www.aviso.oceanobs.com/fileadmin/documents/OSTST/2011/oral/01_Wednesday/Splinter%201%20IP/03%20Smith%20WHFSmith_IP_CS2_2.pdf

[41] F. Boy *et al.*, "Cryosat processing prototype, LRM and SAR processing on CNES side and a comparison to DUACS SLA," in *Proc. OSTST Meet.*, Venice-Lido, Italy, Sep. 22–29, 2012, pp. 1–24. [Online]. Available: http://www.aviso.oceanobs.com/fileadmin/documents/OSTST/2012/oral/02_friday_28/02_instr_processing_II/02_IP2_Boy.pdf

[42] D. Wingham *et al.*, "Cryosat: A mission to determine the fluctuations in Earth's land and marine ice fields," *Adv. Space Res.*, vol. 37, no. 4, pp. 841–871, Jul. 2006.

**Jean-Yves Tourneret** (SM'08) received the Ingénieur degree in electrical engineering from the Ecole Nationale Supérieure d'Electronique, d'Electrotechnique, d'Informatique, d'Hydraulique et des Télécommunications (ENSEEIHT) de Toulouse, Toulouse, France, in 1989 and the Ph.D. degree from the National Polytechnic Institute of Toulouse, Toulouse, in 1992.

He is currently a Professor with the University of Toulouse (ENSEEIHT) and a member of the Toulouse Research Institute in Information Technology Laboratory (UMR 5505 of the Centre National de la Recherche Scientifique). His research activities are centered around statistical signal and image processing with a particular interest to Bayesian and Markov chain Monte Carlo methods.

Dr. Tourneret has been involved in the organization of several conferences, including the European Conference on Signal Processing EUSIPCO'02 (Program Chair), the International Conference ICASSP'06 (plenaries), the Statistical Signal Processing Workshop SSP'12 (international liaisons), the International Workshop on Computational Advances in Multi-Sensor Adaptive Processing CAMSAP 2013 (local arrangement), and the Statistical Signal Processing Workshop SSP'2014 (special sessions). He was the General Chair of the CIMI workshop on optimization and statistics in image processing hold in Toulouse in 2013. He has been a member of different technical committees, including the Signal Processing Theory and Methods committee of the IEEE Signal Processing Society (during 2001–2007 and since 2010). He has been serving as an Associate Editor for the IEEE TRANSACTIONS ON SIGNAL PROCESSING (during 2008–2011) and *Signal Processing* (since July 2013).

**Abderrahim Halimi** (S'11–M'14) received the Eng. degree in electronics from the National Polytechnic School of Algiers, Algiers, Algeria, in 2009 and the M.Sc. and Ph.D. degrees in signal processing from the Institut National Polytechnique de Toulouse, Toulouse, France, in 2010 and 2013, respectively.

He is currently a Postdoctoral Researcher with the Institut de Recherche en Informatique de Toulouse, University of Toulouse, Toulouse. His research activities focus on statistical signal and image processing, with a particular interest in Bayesian inverse problems with applications to hyperspectral imaging and altimetry.

**Francois Boy** received the Eng. degree in physics from the Ecole Centrale Marseille, Marseille, France, in 2005 and the M.S. degree in electronics from the University of Toulouse, Toulouse, France, in 2006.

He is currently with the Centre National d'Etudes Spatiales, Toulouse, in the altimetry and radar department. His research activities are centered around processing methods for SAR/Doppler altimetry systems (CRYOSAT and Sentinel-3 missions).

**Corinne Mailhes** (M'87) received the Ph.D. degree in signal processing from the University of Toulouse, Toulouse, France, in 1990.

She is currently a Professor with the University of Toulouse, a member of the Institut de Recherche en Informatique de Toulouse, and the Director of the Telecommunications for Space and Aeronautics Laboratory. Her research interests include statistical signal processing, with particular interests in spectral analysis, parameter estimation, and biomedical signal processing.

**Thomas Moreau** received the Ph.D. degree in planetary and space physics from the University of Toulouse, Toulouse, France, in 2003.

He has been working on a number of space instrument projects, developing numerical methods to simulate the performances of the head of detectors, and taking part at the full calibration process. Since 2008, he has been conducting many studies devoted to the analysis and development of methods and algorithms for processing both conventional pulse-limited and SAR altimetry data within the Oceanography Division of Collecte Localisation Satellites, Toulouse.